Strain gradient plasticity analysis of the strength and ductility of thin metallic films using an enriched interface model

C. Brugger [a,*], M. Coulombier [a], T.J. Massart [b], J.-P. Raskin [a], T. Pardoen [a]

[a] Institute of Mechanics, Materials and Civil Engineering, Université catholique de Louvain, 1348 Louvain-la-Neuve, Belgium
[b] Université Libre de Bruxelles, Building, Architecture & Town Planning Dept. (BATir) CP 194/02, Avenue F.D. Roosevelt 50, 1050 Bruxelles, Belgium

Received 29 March 2010; received in revised form 5 May 2010; accepted 6 May 2010
Available online 17 June 2010

Abstract

The mechanical response of thin metallic films is simulated using a two-dimensional strain gradient plasticity finite-element model involving grain boundaries in order to investigate the effect of the thickness, grain shape and surface constraint on the strength, ductility and back-stress. The grain boundaries and surface layers are modeled as initially impenetrable to dislocations while allowing for relaxation at a critical stress level. The model captures the variation of the strength with grain size, film thickness, and with the presence or not of constraining surface layers, in agreement with experimental results on Al and Cu films. A decrease in the uniform elongation is predicted with decreasing film thickness due to a loss of strain-hardening capacity and the possible presence of imperfections. These two effects dominate over the stabilizing contribution of the plastic strain gradients. Accounting for the relaxation of the interface constraint affects the magnitude of the back-stress as well as the drop in ductility.

Keywords: Thin films; Strain gradient plasticity; Size effects; Ductility; Bauschinger effect

1. Introduction

The low ductility of thin metallic films is a key issue in many applications, including flexible electronic systems [1–3], some micro- and nano-electromechanical systems (MEMS/NEMS) devices [4,5], or in thin coatings which must sustain forming operations after deposition or resist scratching [6]. Although the origin of the increased strength when thickness decreases has been widely investigated using both experimental and computational approaches [7–15], a proper understanding and modeling of the limited strain-hardening capacity leading to the often mediocre resistance to plastic localization of thin films is still lacking.

The dislocation motion in thin metallic films is affected by the high density of interfaces and the large surface-to-volume ratio. The interactions of dislocations with grain boundaries, with interfaces between the film and the substrate or with another film, as well as with possible oxide layers at the surface, induce the coexistence of multiple mechanisms such as blocking, annihilation, emission, reflection and transmission, depending on the stress level and on the character/structure of the interface. As a result, the density of dislocation barriers is related to both the grain size d and the sample thickness h. An empirical relationship describing the evolution of the strength with these two parameters has been proposed by de Boer et al. [8] based on experimental data collected by Venkatraman and Bravman [10] for Al–0.5%Cu thin films sandwiched between an SiO_2 layer on the substrate side and a 65 nm thick anodic oxide film intentionally grown on the surface: $\sigma_{ys} = m/h + K/\sqrt{d}$, where $m = 83\,\text{MPa}\,\mu\text{m}$ and $K = 100\ \text{MPa}\sqrt{\mu\text{m}}$. Additional effects related to the presence of material, geometrical imperfections or growth twins, to grain growth mechanisms, to the strength of the oxide layer, and to the strain rate-sensitivity, can also have a first-order impact on the ductility (e.g. [16]).

In order to capture the different size effects affecting both the strength and ductility in thin films, a finite-element model has been developed relying on a finite-strain

* Corresponding author. Tel.: +32 10 47 24 90; fax: +32 10 47 40 28.
E-mail address: charles.brugger@uclouvain.be (C. Brugger).

1359-6454/$36.00 © 2010 Acta Materialia Inc. Published by Elsevier Ltd. All rights reserved.
doi:10.1016/j.actamat.2010.05.021

implementation of the strain gradient plasticity theory developed by Fleck and Hutchinson [17] for the behavior of the grain interior. Cohesive zones are used to represent the interface layers, together with evolving higher-order boundary conditions at the frontier with the grain interior (see Fig. 1). The interface layers are extremely thin, of the order of a few atomic spacings, depending on the type of interface considered (grain boundary, interface with an oxide layer, interphase) with a structure, and thus a response, different from that of the grain interior. The interface layers are considered to be initially impenetrable to dislocations. This is enforced by constraining the plastic strain rate at the interfaces between the grain interior and the layer. When applying the load, the grain interior starts deforming plastically while the interface layers remain elastic. The strength of the near-interface regions increases rapidly due to the large local plastic strain gradients resulting from the higher-order boundary conditions, generating also large back-stress levels within the grain interior. When the stress on an interface reaches a critical value, the different mechanisms of transmission, nucleation and/or sinking of dislocations start being activated. This is empirically modeled by relaxing the constraint on both sides of the interface layer, and letting the plastic flow develop within it. The back-stress then also partially relaxes. From that point on, the confinement is not explicitly enforced through the higher-order effect, and the plastic flow is only controlled by the classical behavior of the interface layer represented by a simple linear hardening law. The slope of the classical hardening law of the interface layer phenomenologically represents the resistance to dislocation motion imposed by the mechanisms occurring inside the interface layer and the evolving structure of the interface. A similar model has been applied to address the grain-size-dependent strength and ductility of ferrite [18] and the behavior of transformation-induced plasticity (TRIP)-assisted multiphase steels [19].

The objective of this paper is to investigate the relationships between the strength and ductility, and the main microstructural parameters of thin metallic films. The focus will be on the 0.2% offset yield stress and on the uniform elongation, defined as the strain at which elastic unloading first occurs, indicating plastic localization. The grain size and sample thickness condition the respective influence of the presence of grain boundaries, and interfaces with the substrate or with possible oxide layers. The influence of imperfections and of the grain size distribution on the onset of necking will also be addressed. The predictions are compared with the experimental data of Venkatraman and Bravman [10] (see above), Xiang and Vlassak [20], as well as with uniaxial tensile tests performed on 200 and 375 nm thick aluminum samples using a novel dedicated on-chip tensile testing technique [21,22].

Section 2 presents the constitutive model and numerical procedures. Section 3 addresses the influence of the key parameters on both the strength and ductility, and validates the model by comparison with the experimental results. The paper ends with conclusions and perspectives.

2. Model and numerical procedures

2.1. Model

The grain interior response (see Fig. 1) is modeled using the strain gradient plasticity theory proposed by Fleck and Hutchinson [17], extended to finite-strains by Niordson

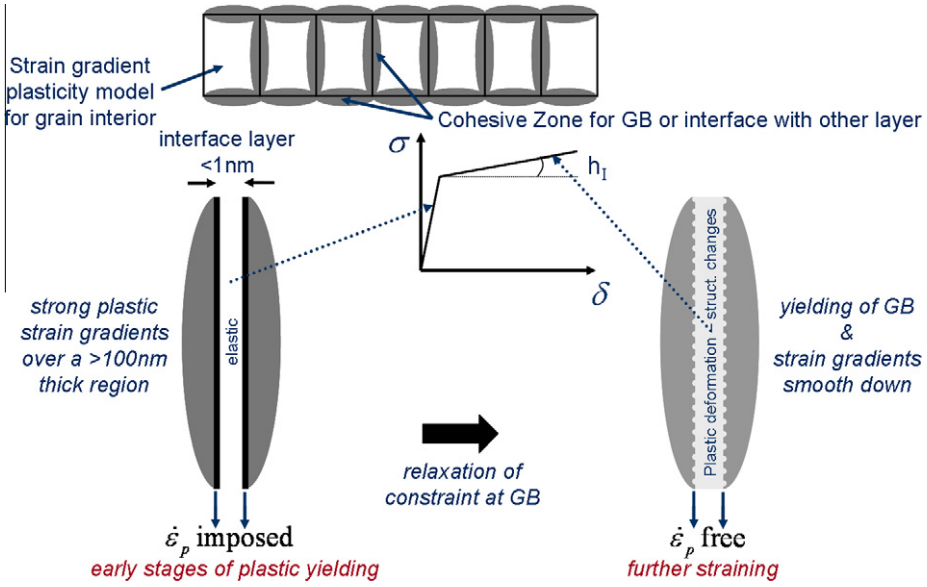

Fig. 1. Schematic description of the 2-D plane-strain model for the polycrystalline thin film based on a strain gradient plasticity description of the grain interior and cohesive zone representation of the interface layers (grain boundaries and interfaces with other layers) involving, on both sides, evolving higher-order boundary conditions.

et al. [23,24]. The gradient-hardening effect is introduced through a generalized effective plastic strain rate $\dot{E}_p$, defined in terms of the rate of the conventional J_2 definition of the effective plastic strain $\dot{\varepsilon}_p = \sqrt{\frac{2}{3}\dot{\varepsilon}^p_{ij}\dot{\varepsilon}^p_{ij}}$ (where $\dot{\varepsilon}^p_{ij}$ are the components of the plastic strain rate tensor), of its spatial gradients $\dot{\varepsilon}_{p,i}$, and, in the most simple version, of one internal length parameter l_* as:

$$\dot{E}^2_p = \dot{\varepsilon}^2_p + l^2_* \dot{\varepsilon}_{p,i}\dot{\varepsilon}_{p,i} \tag{1}$$

Both terms in Eq. (1) relate respectively to the strengthening brought by the motion of the statistically stored dislocations (SSDs) and to geometrically necessary dislocations (GNDs) [25]. Physically, the parameter l_* controls the relative contribution of both the plastic strains and plastic strain gradients assuming that SSDs and GNDs affect the hardening equally [25]. The plastic strain rate is given by the usual flow rule $\dot{\varepsilon}^p_{ij} = \dot{\varepsilon}_p \frac{3}{2} s_{ij}/\sigma_{(e)} = \dot{\varepsilon}_p m_{ij}$, where s_{ij} are the components of the deviatoric part of the Cauchy stress tensor σ_{ij} and $\sigma_{(e)}$ is the von Mises stress. Using an independent plastic strain field on equal footing with the displacement field, the principle of virtual work expressed in the current configuration is:

$$\int_V (\sigma_{ij}\delta\dot{\varepsilon}_{ij} + (Q - \sigma_{(e)})\delta\dot{\varepsilon}_p + \tau_i\delta\dot{\varepsilon}_{p,i})\,\mathrm{d}V = \int_S (T_i\delta\dot{u}_i + t\delta\dot{\varepsilon}_p)\mathrm{d}S \tag{2}$$

where ε_{ij} is the total strain, Q the stress measure work-conjugate to the conventional effective plastic strain, τ_i is the higher-order stress conjugate to the spatial gradient of the conventional effective plastic strain, T_i is the conventional traction at the boundary of the solid, and t is the higher-order traction acting at the boundary of the plastically deforming region. The description of the finite-strain formulation and the detailed finite-element implementation of this strain gradient plasticity framework can be found in Refs. [23,24] based on relations from Ref. [26] for the finite-strain setting. The implementation is purely incremental, which means that the variation in displacement and effective plastic strain are the unknowns at each step.

A number of recent contributions have examined the influence of interface plasticity on the flow behavior of polycrystals, including the impact of a change in the confining conditions on the evolution of plastic strain gradients along the deformation history [27–31]. In the present contribution, higher-order confinement is considered only at the pre-existing fixed boundaries (surfaces and grain boundaries), and not at the moving elastoplastic boundaries.

The hardening modulus $h(E_p)$ is described by a Voce-type law, which is known to provide a physically realistic description of stage III hardening [32], as:

$$h(E_p) = \frac{\partial\sigma_y}{\partial\varepsilon_P} = \Theta_0 - \beta(\sigma_y(E_p) - \sigma_0) \tag{3}$$

Note that the hardening modulus is evaluated at the generalized plastic strain E_p, in order to include all contributions to hardening from both SSDs and GNDs.

The interface layer behavior (grain boundaries or interfaces with surrounding material layers) is described using a cohesive zone (CZ) model. As sketched in Fig. 1, the behavior is first elastic with the following relationship:

$$\begin{bmatrix}\tau\\ \sigma\end{bmatrix} = \begin{bmatrix}E/w & 0\\ 0 & G/w\end{bmatrix}\begin{bmatrix}\Delta u_t\\ \Delta u_n\end{bmatrix} \tag{4}$$

where w is the initial thickness of the interface layer (typically $w < 1$ nm), E and G are the Young's and shear modulus, respectively, and Δu_t and Δu_n represent the tangential and normal relative displacement over the thickness w, respectively. For the sake of simplicity, the elastic parameters of the CZ are considered similar to the grain interior.

Now, the key ingredient, more than the traction separation response of the interface layer, is the presence of two interfaces on both sides of the CZ. Higher-order boundary conditions are applied on these interfaces. The plastic flow is initially constrained by imposing the condition $\dot{\varepsilon}_p = 0$ via a penalty term at the boundary of the grain interior. This results in the development of strong plastic strain gradients in the grain interior. The effect on the overall strength depends on the magnitude of the plastic strain gradients and on the intrinsic length l_* compared to the grain size d and thickness h. These higher-order conditions are more important regarding the response of the grain aggregate than the CZ behavior.

Upon further straining, the confinement condition can be modified [19,33] based on a condition on the local (conventional) stress carried by the CZ. The condition for relaxing the higher-order confining effect is formulated in terms of the CZ von Mises stress as:

$$\sigma_{eq} = \sqrt{\sigma^2 + 3\tau^2} \geqslant \sigma_{IRS} \tag{5}$$

where σ_{IRS} is the phenomenological parameter governing the relaxation of the constraint, termed the interface relaxation stress.

The initial elastic behavior is followed by an empirical linear hardening response of the interface layer (see Fig. 1):

$$\sigma_{y,\mathrm{CZ}}(\kappa) = \sigma_{0,\mathrm{CZ}} + h_I\kappa \tag{6}$$

where $\sigma_{0,\mathrm{CZ}}$ is the initial yield stress of the CZ, κ is the hardening parameter taken as the equivalent plastic opening of the CZ, and h_I is the hardening slope. The plastic behavior of the CZ representing the interface layer is assumed to follow an associated flow rule. For simplicity, and in the absence of a physical model to distinguish them, σ_{IRS} and $\sigma_{0,\mathrm{CZ}}$ are assumed to be equal in this study.

2.2. Numerical procedures

Uniaxial tensile tests of thin free-standing films made of a columnar grain structure are simulated in 2-D. The thin films can be modeled using either plane-strain or plane-stress conditions. In 2-D plane stress, the films are described as collections of grains, while neglecting the stress variation over the thickness. In 2-D plane-strain, the films are represented as ribbons of rectangular grains, the strain variation along

the width being neglected, such as for instance in the dislocation dynamics simulations by Nicola et al. [12,34,35]. In this paper, only predictions obtained with the 2-D plane-strain model are described in order to address the influence of the thickness or the presence of a substrate or oxide layer on the surfaces. In 2-D plane-strain, necking takes place over a region scaling with the thickness.

The grains are modeled as identical rectangles, with a thickness h (height dimension), and a grain size d (in plane dimension). Two different representative volume elements are considered, depending on whether or not plastic localization is simulated. For the small strain calculations without necking (see the results given in Figs. 4, 5 and 8) only two half-grains surrounding a grain boundary are modeled (see Fig. 2a). Periodic boundary conditions simulate plane-strain tension in a direction perpendicular to the grain boundary. For large strain calculations, needed to address necking, a ribbon made of 20 grains is simulated. For symmetry reasons, it is sufficient to model only one-quarter of the ribbon (see Fig. 2b). In order to simulate necking, an imperfection η is introduced in the central grain and the boundary conditions are no longer periodic. The imperfection consists of a smaller initial flow stress equal to $(1-\eta)\,\sigma_0$, where σ_0 is the initial flow stress of the other grains. A few calculations are also performed using normal grain size distributions (see Fig. 2c) with a mean $d = l_*$ and a standard deviation $\Delta d = 0.2 l_*$. Normalized grain sizes range between $d/l_* = 0.32$ and 1.44.

The bulk material elastic behavior is given by the Young's modulus E and Poisson ratio ν. The plastic behavior is described by the Voce law [32] characterized by σ_0, Θ_0 and β_0. The strain gradient plasticity model involves the internal length l_*. Three cases are considered: a single free-standing film with free surfaces ($n = 0$); a film with one constrained surface ($n = 1$); or a film with two constrained surfaces ($n = 2$). For the sake of simplicity, the interface layer behaviors are characterized by the same two parameters: the interface relaxation stress σ_{IRS}, and the effective hardening h_I. Although the interface relaxation stress is the same for all cohesive zones, the stress undergone by each CZ depends on its location and relaxation does not occur simultaneously on all interface layers. Note that the surrounding substrate, adjacent film or oxide layer are not modeled, but only the interface layers with them. Hence, the effect of the long-range stress fields induced by dislocation accumulation in a plastically deforming substrate is not, for instance, taken into account. Furthermore, in the case of the finite-strain analysis, the simulations only make sense for free-standing films with or without oxide layers. The presence of the substrate or of an adjacent film would of course very much affect the localization problem [36–39].

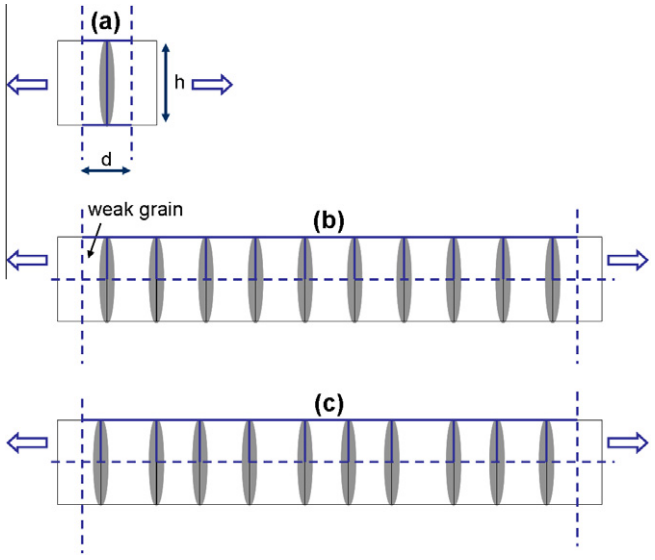

Fig. 2. 2-D plane-strain descriptions of the polycrystalline thin film: two half-grains surrounding a grain boundary (a), 20 grain ribbon (quarter symmetry) without (b) or with grain size distribution (c).

Dimensional analysis shows that the 0.2% offset yield stress σ_y and uniform strain ε_u depend on the following parameters:

$$\frac{\sigma_y}{\sigma_0} = F\left(\underbrace{\frac{E}{\sigma_0}, \nu, \frac{\Theta_0}{\sigma_0}, \beta_0}_{\text{behavior of the coarse grain material}} , \underbrace{\frac{d}{l_*}, \frac{h}{l_*}, \eta, n}_{\text{thin film parameters}} , \underbrace{\frac{\sigma_{IRS}}{\sigma_0}, \frac{h_I}{E}}_{\text{interface parameters}} \right) \tag{7}$$

$$\frac{\varepsilon_u}{\varepsilon_u^{\eta\to 0}} = F\left(\underbrace{\frac{E}{\sigma_0}, \nu, \frac{\Theta_0}{\sigma_0}, \beta_0}_{\text{behavior of the coarse grain material}} , \underbrace{\frac{d}{l_*}, \frac{h}{l_*}, \eta, n}_{\text{thin film parameters}} , \underbrace{\frac{\sigma_{IRS}}{\sigma_0}, \frac{h_I}{E}}_{\text{interface parameters}} \right) \tag{8}$$

The uniform strain ε_u is the largest strain for which no elastic unloading is detected in the film. It is a lower bound estimate of the ductility. The four parameters describing the grain interior behavior are kept constant: $E/\sigma_0 = 1167$, $\nu = 0.3$, $\Theta_0/\sigma_0 = 9$, $\beta_0 = 13.5$ [40]. These parameters are representative of pure aluminum. The influence of the other parameters is considered with variations around one master case set of parameters which consists of the normalized thickness $h/l_* = 1$, normalized grain size $d/l_* = h/l_*$, imperfection $\eta = 1\%$ (when applicable), and no constrained surfaces, i.e. $n = 0$. The two parameters related to the response of the interface layers are the normalized interface relaxation stress σ_{IRS}/σ_0, set to a very high value equal to 1000 (i.e. impenetrable interface), and the normalized effective hardening $h_I/E = 1$ (which has no effect on the response as the CZ remains elastic in all simulations performed with the master case). If not specified, a parameter is set to its master case value.

3. Results and discussion

3.1. Contributions of the different interface layers to strengthening

Fig. 3 presents the influence of the higher-order boundary conditions on the normalized engineering stress σ/σ_0 vs.

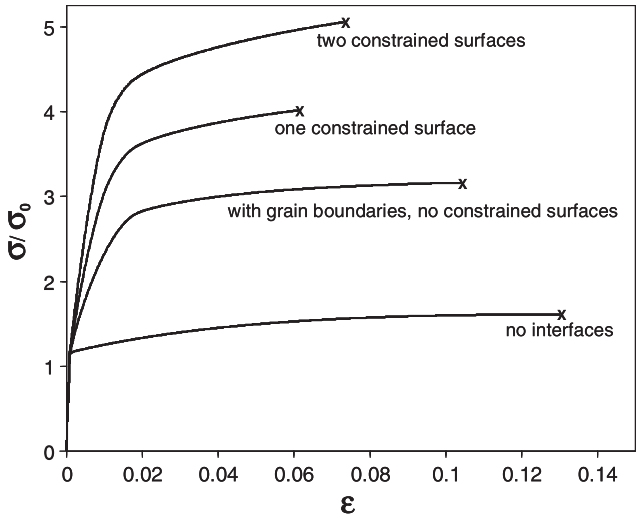

Fig. 3. Normalized engineering stress–engineering strain curves: effect of imposing higher-order boundary conditions on the grain boundaries only, as well as on one or two surfaces.

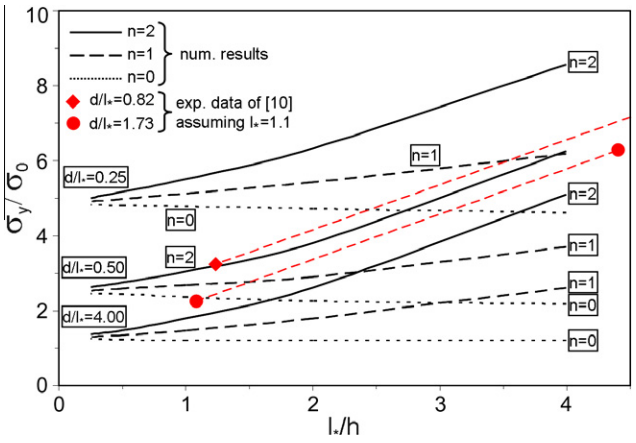

Fig. 4. Variation of the normalized yield stress as a function of the inverse of the normalized thickness, for no ($n = 0$, dotted lines), one ($n = 1$, dashed lines) or two ($n = 2$, continuous lines) constrained surfaces, and for three values of the normalized grain size d/l_*. Symbols ♦ and ● are the experimental data from Venkatraman [10] assuming $l_* = 1.1$ μm (For interpretation of the references to colour in this figure legend, the reader is referred to the web version of this article.).

strain ε curves obtained with the finite-strain ribbon model (see Fig. 2b). Four configurations are considered: homogeneous (without any interface); no constrained surface ($n = 0$, i.e. only grain boundaries); one constrained surface ($n = 1$); and two constrained surfaces ($n = 2$). The curves are stopped when plastic localization is detected ($\varepsilon = \varepsilon_u$). The introduction of interface layers induces additional plastic strain gradients in the film contributing to an enhanced strengthening. All the interfaces contribute to the strengthening, the effect of grain boundaries being almost equal to that of two constrained surfaces. Note that this is only true for equiaxed grains, where the total length of vertical and horizontal interfaces is the same. The influence of the grain shape on the relative contributions of the grain boundaries and of the constrained surfaces will be addressed in the next subsection. A loss of ductility occurs with increasing strength, except for the fully confined conditions ($n = 2$). Note that strain gradients also affect the response of the homogeneous film, but only when heterogeneities start developing, i.e. after the onset of plastic localization (see further). The results of Fig. 3 provide the general picture of the different phenomena of interest in this study, which are now investigated individually in more detail.

3.2. Yield strength

A more in-depth analysis of the yield strength is performed using the simple two-grain model (see Fig. 2a). Fig. 4 shows the variation of the normalized yield stress σ_y/σ_0 as a function of the inverse of the normalized thickness l_*/h for thin films without constrained surface ($n = 0$), with one ($n = 1$), or two ($n = 2$) constrained surfaces, and for three values of the normalized grain size d/l_*. For a given normalized grain size d/l_*, the thickness effect depends on the presence or not of dislocation barriers on the surfaces. In the absence of constrained surfaces ($n = 0$), the strength decreases slightly with decreasing thickness at constant grain size. This effect is reasonable considering that, in reality, it is easier for the dislocations to escape from the film when the grains are flat. However, for films involving one ($n = 1$) or two ($n = 2$) constrained surfaces, i.e. oxides or other layers, the strain gradients induced by the higher-order boundary conditions lead to a thickness-dependent strengthening. This effect has been demonstrated experimentally, for instance, by Vlassak and co-workers [13,20] (we will come back to this comparison in the final section). The thinner the film, the larger the strengthening. However, these surface barriers to plastic flow on the lower and upper surfaces have almost no influence once the thickness is larger than $4l_*$ (i.e. $l_*/h < \frac{1}{4}$). Indeed, the contribution of the large plastic strain gradients near the surfaces becomes small when averaging the overall behavior. As a matter of fact, for a given normalized thickness h/l_* and a given number of constrained surfaces n, the classical grain size effect is observed: the smaller the grain size, the larger the yield strength, in agreement with the Hall–Petch effect [41,42]. The fact that the grain boundaries are perfectly vertical in this model and perpendicular to the main loading directly affects the predictions and leads to almost no coupling between d and h (the variations with l_*/h are independent of d/l_*). This is in agreement with the empirical relationship given in the introduction [8]. Introducing a more realistic distribution of grain boundaries in 3-D would probably introduce some degree of thickness dependence.

Fig. 4 also allows the influence of the grain shape to be addressed. In the absence of constrained surface ($n = 0$), since the strength depends almost exclusively on the grain size, elongated grains are stronger than equiaxed and flat grains. However, the strengthening effect associated with

the presence of constrained surfaces is larger in flat grains compared to equiaxed and elongated grains. For instance, with two constrained surfaces ($n = 2$), elongated ($h/l_* = 4$, $d/l_* = 0.25$), equiaxed ($h/l_* = 2.125$, $d/l_* = 2.125$) and flat ($h/l_* = 0.25$, $d/l_* = 4$) grains, having the same total length of interfaces in the plane of deformation, show normalized yield stresses equal to $\sigma_y/\sigma_0 = 5.01$, 1.56 and 5.10, respectively. The lower strength is obtained for the equiaxed grains, where grain boundaries and constrained surfaces contribute almost equally to the strengthening induced by the strain gradients. For the elongated and flat grains, the smaller the grain size (respectively the thickness), the more effective are the vertical (respectively horizontal) interfaces in terms of strengthening.

Fig. 5 presents the influence of the normalized interface relaxation stress σ_{IRS}/σ_0 and effective hardening h_I/E on the normalized engineering stress–strain curves, for a normalized thickness and grain size $h/l_* = d/l_* = 0.5$ (no constrained surface, i.e. $n = 0$). The smaller the interface relaxation stress, the sooner the curves depart from the "impenetrable" interface limit ($\sigma_{IRS} = \infty$). As soon as grain boundary relaxation occurs somewhere in the film, the overall behavior starts depending on the response of the interface layers. Therefore, the smaller the relaxation stress, the larger the influence of the effective hardening of the interface layer. Again, the simplified ribbon-type geometry artificially amplifies the grain boundary effect. Fig. 5 shows that the behavior can become perfectly plastic for smaller values of σ_{IRS} and h_I. The connection between the interface relaxation stress and the physical mechanisms remains an open question and probably requires information derived from atomistic calculations (e.g. [43–45]). Note that these two parameters have an influence on the apparent work hardening, but not on the 0.2% offset yield stress for the range of parameters tested here.

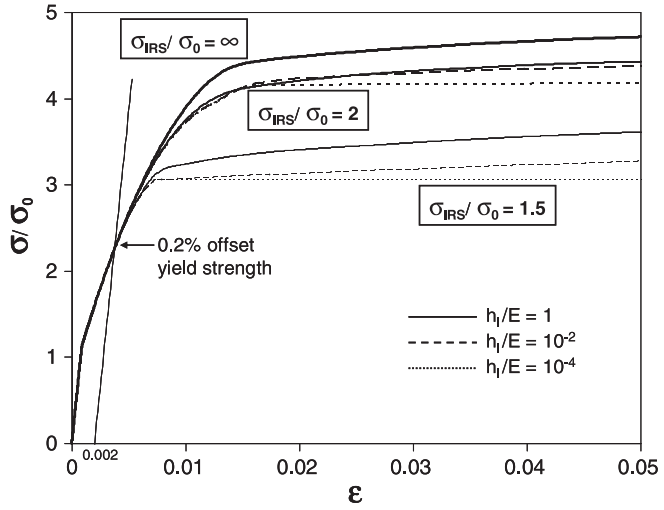

Fig. 5. Effect of the normalized effective hardening (dotted lines: $h_I/E = 10^{-4}$, dashed lines: $h_I/E = 10^{-2}$, continuous lines: $h_I/E = 1$) on the normalized engineering stress–strain curves for three values of the normalized interface relaxation stress σ_{IRS}/σ_0.

3.3. Strain hardening

Strain hardening and plastic localization have been addressed using finite-strain simulations performed with the ribbon model (see Fig. 2b). Fig. 6a presents the influence of the normalized thickness h/l_* on the normalized engineering stress–strain curves for homogeneous or polycrystalline free-standing thin films with no constrained surface. Note that for the polycrystalline films, the grain size is equal to the thickness ($d/l_* = h/l_*$), and the grain boundaries are modeled as impenetrable interfaces ($\sigma_{IRS}/\sigma_0 = \infty$). The thickness can have two opposite effects on the ductility depending on the presence or not of grain boundaries. In homogeneous films, the thinner the film, the larger the magnitude of the plastic strain gradients, hence the ductility. Plastic strain gradients tend to stabilize plastic localization by providing additional strengthening

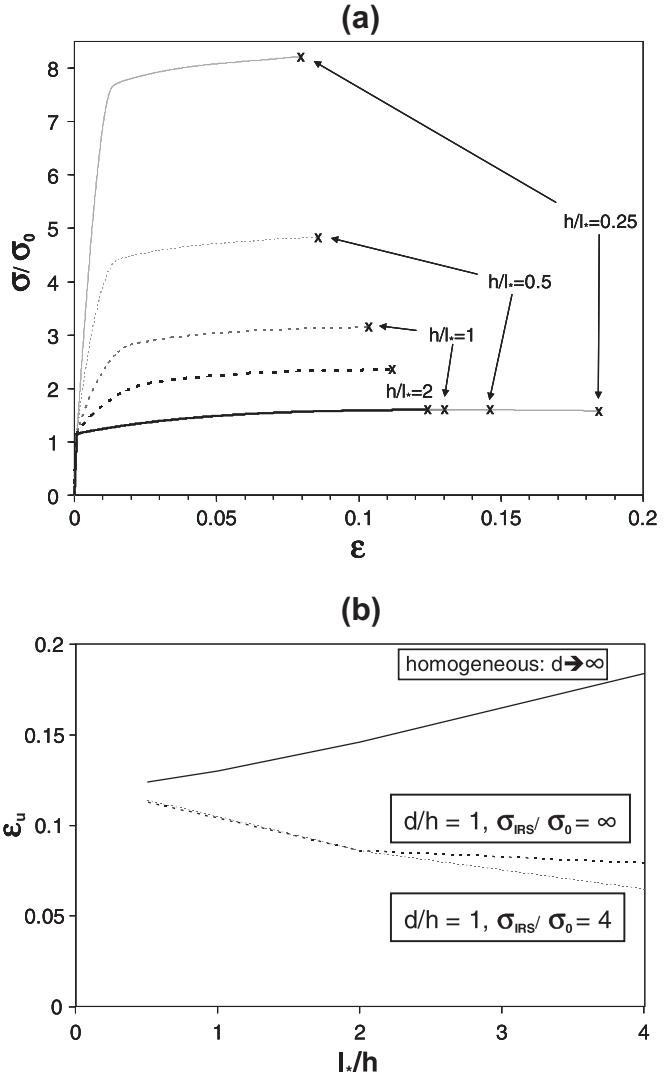

Fig. 6. Effect of the normalized thickness h/l_* on (a) the normalized engineering stress–strain curve and (b) on the uniform elongation for homogeneous (continuous lines) or polycrystalline (dotted lines) free-standing films with or without grain boundary relaxation.

to the region where necking initiates. This effect has been discussed by Niordson and Tvergaard [23]. In polycrystalline films, the ductility decreases with decreasing thickness. This drop in ductility associated with the size-induced strengthening has been shown experimentally directly or indirectly; see many examples of very small ductility reported for thin films [46–48]. A decrease in the ductility is captured by the model, though there is no dramatic drop. Now, allowing for grain boundary relaxation through decreasing the associated stress σ_{IRS} leads to a more significant loss of ductility, as shown in Fig. 6b, where the uniform strain of free-standing polycrystalline thin films is plotted as a function of the inverse of the normalized thickness l_*/h for $\sigma_{IRS}/\sigma_0 = \infty$ or 4. The relaxation of the higher-order boundary conditions thus has little influence on the yield strength, but has an impact on the loss of ductility for very thin films.

Fig. 7 presents the variation of the normalized uniform elongation $\varepsilon_u/\varepsilon_u^{\eta\to 0}$ as a function of the imperfection η, allowing or not for grain boundary relaxation, i.e. $\sigma_{IR}/\sigma_0 = \infty$ or 4. In bulk materials, the ductility decreases very significantly in the presence of imperfections [49]. The imperfection sensitivity in thin films is not expected to be as large as in bulk materials due to strain gradient effects. In Fig. 7, very limited imperfection sensitivity is predicted without grain boundary relaxation: a 10% imperfection leads to less than 20% loss of ductility. With relaxation of the grain boundary confinement, a much larger decrease by 50% of the ductility is predicted by the model. The loss of ductility depends thus heavily on the grain boundary relaxation σ_{IRS}/σ_0. Indirect evidence of significant imperfection sensitivity in thin films has been recently provided [22], thus justifying the use of a limited value of σ_{IRS} in the context of the present model to capture this effect (see last section). Thin films are more susceptible to imperfections than bulk material, as a result of the roughness, grain boundary grooving or the columnar grain structure (one grain over the thickness).

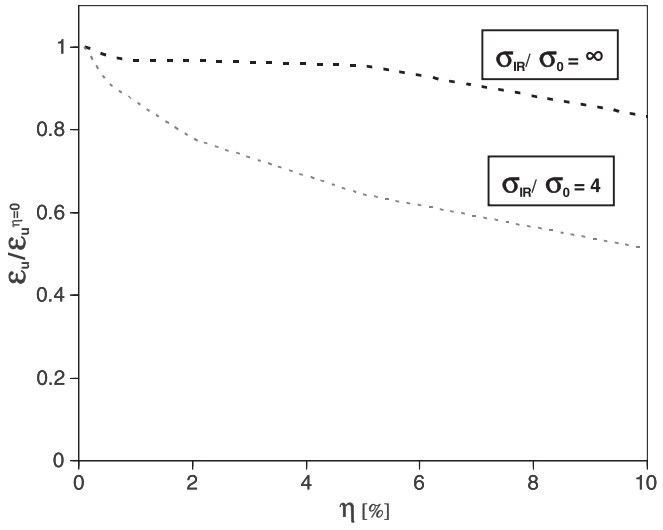

Fig. 7. Variation of the normalized uniform elongation as a function of the imperfection size for polycrystalline free-standing films with or without grain boundary relaxation.

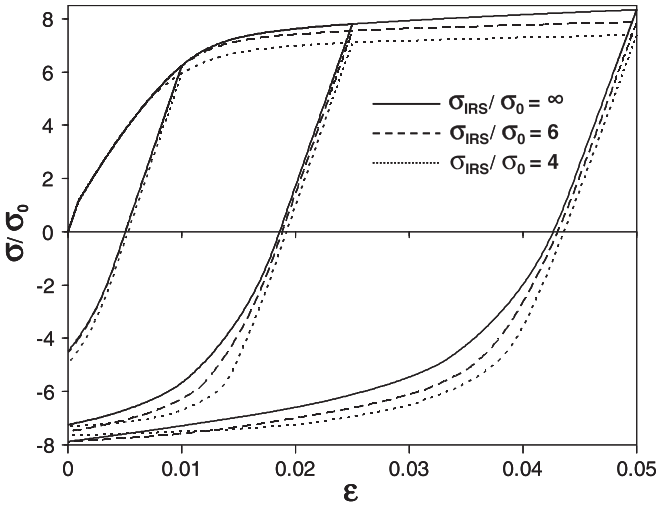

Fig. 8. Bauschinger effect: influence of the normalized grain boundary relaxation stress σ_{IRS}/σ_0 on the normalized engineering stress–strain curve, in a model with grain boundary and constrained surfaces.

3.4. Bauschinger effect

Fig. 8 shows the influence of the interface relaxation stress σ_{IRS}/σ_0 on the normalized engineering stress–strain curve, for thin films with two constrained surfaces ($n = 2$), and for a thickness and grain size $h/l_* = d/l_* = 0.5$. When increasing the pre-strain, the level of compressive stress required for reverse plastic flow is decreased. This effect is not observed in the absence of constrained surfaces. The larger the grain boundary relaxation stress, the stronger is the Bauschinger effect. Indeed, the largest back-stresses are generated when no relaxation of the interfaces is allowed, involving the largest possible plastic strain gradients. For larger values of the grain boundary relaxation stress and pre-strain, reverse plastic flow starts under tensile macroscopic stress. The Bauschinger effect is extremely difficult to test experimentally on thin films. As explained in more detail in the last section, Xiang and Vlassak [20] performed reverse-loading experiments by using a modified version of the plane-strain bulge test on Cu thin films, showing but only for passivated films a very significant Bauschinger effect starting under positive stress.

3.5. Grain size distribution

Fig. 9 shows the normalized engineering stress–strain curves obtained for 10 different grain size distributions (see Fig. 2c), compared to the master case involving a single grain size (see Fig. 2b) and no imperfection ($\eta = 0$). The master case gives an upper bound on the strength and on the ductility. Accounting for a grain size distribution induces a slight decrease in the strength and a noticeable loss of ductility. The smallest stress was observed for the

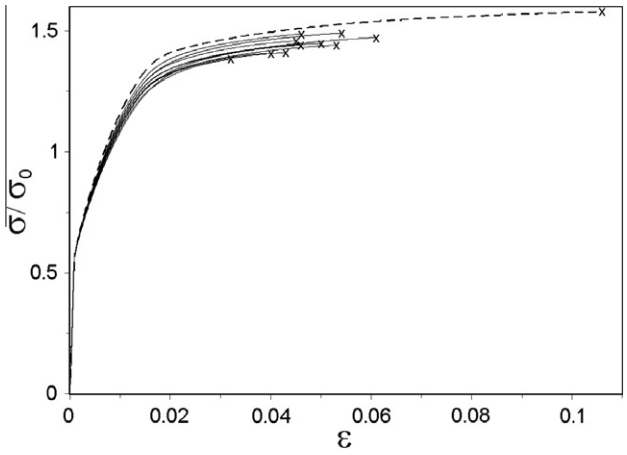

Fig. 9. Effect of 10 different grain size distributions (continuous lines) on the normalized engineering stress–strain curve compared to the master case (dashed line).

distribution involving the largest grain: the uniform strain and corresponding stress are about 60% and 10% lower than the master case, respectively. The largest grain has a major impact on the behavior. It sets the maximum level of strengthening. Again, the 2-D ribbon model artificially amplifies grain distribution effects, as the imperfection is affecting the entire width, which is not the case in reality except for a bamboo-like structure. According to Fig. 4, the yield stress is 10% lower than the master case with the distribution involving the largest grain (with $d/l_* = 1.44$). In fact, this large grain introduces an imperfection in the film equal to $\eta = 10\%$, which is responsible for most of the drop of ductility. According to Fig. 7, it should lead to a 50% drop of the uniform elongation. Even though the 2-D model exaggerates this effect, it reveals the importance of the grain size distribution in the range of sizes ($d < 1$ μm) where the strength is significantly affected by small changes in the dimensions of the microstructure. The grain size distribution is thus a primary source of imperfections controlling the resistance to necking.

3.6. Assessment in terms of experimental data

Several qualitative assessments in terms of experimental data have been mentioned in the previous sections and are now analyzed in more detail. First, the variation of the 0.2% offset yield stress as a function of the thickness and grain size has been addressed in Fig. 4. A comparison with experimental data requires specifying a value for the internal length l_*. The best agreement with Venkatraman and Bravman [10] results for Al thin films with two constrained surfaces (one substrate and one 65 nm thick oxide) and for two mean grain sizes $d = 0.9$ and 1.9 μm is found using $l_* = 1.1$ μm, i.e. $d/l_* = 0.82$ and 1.73. These results have been added in Fig. 4. The evolution with l_*/h closely parallels the predictions of the model using $n = 2$. By interpolating through the data, the experimental results match the predictions for $d/l_* = 0.43$ and $d/l_* = 0.72$, which are lower than the experimental values $d/l_* = 0.82$ and $d/l_* = 1.73$. The criterion used experimentally to determine σ_y might, however, be an issue: slightly increasing the offset value used to define σ_y would lead to larger values of the predicted σ_y (see Fig. 5), in closer agreement with the experimental results.

Xiang and Vlassak [20] measured the effect of a passivation layer on the yield stress of free-standing copper thin films with thicknesses ranging from $h = 0.34$ to 4.2 μm, using the plane-strain bulge test. Submicron films were sputter-deposited with average grain sizes ranging from $d = 0.33$ to 0.54 μm, whereas thicker films were electroplated with an average grain size $d = 1.5$ μm. In order to characterize the effect of the passivation layer, a strengthening factor S was defined as:

$$S = \sigma_y^{n=1}/\sigma_y^{n=0} \tag{9}$$

where $\sigma_y^{n=1}$ and $\sigma_y^{n=0}$ are the yield stresses for a film with one or no passivated surface, respectively. Fig. 10 shows the variation of S as a function of the thickness h for both sputtered and electroplated films. The predictions of the model shown in Fig. 4 are converted in S values and plotted in Fig. 10 using $d/l_* = 1.5$ (i.e. $d = 1.5$ μm and $l_* = 1$ μm) on Fig. 4. Although the results plotted on Fig. 4 were obtained using parameters representative of pure Al, the comparison with the results on Cu is very good, in terms of capturing the relative effect on the strengthening of constraining or not the plastic flow at one film surface.

Xiang and Vlassak [20] also observed a large Bauschinger effect in the passivated submicron Cu films, with reverse plastic strain increasing linearly with the pre-strain. The results of Fig. 8 were used to determine the back-stress σ_b, defined as:

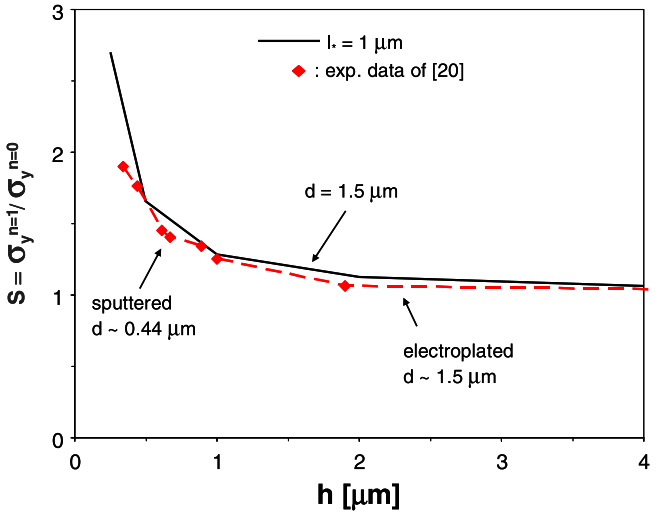

Fig. 10. Variation of the strengthening factor S resulting from constrained plastic flow at one film surface as a function of the film thickness h. The symbols are the experimental data measured by Xiang and Vlassak [20]. The continuous line is the prediction of the model for $d = 1.5$ μm and $l_* = 1$ μm (and all other parameters of the master case).

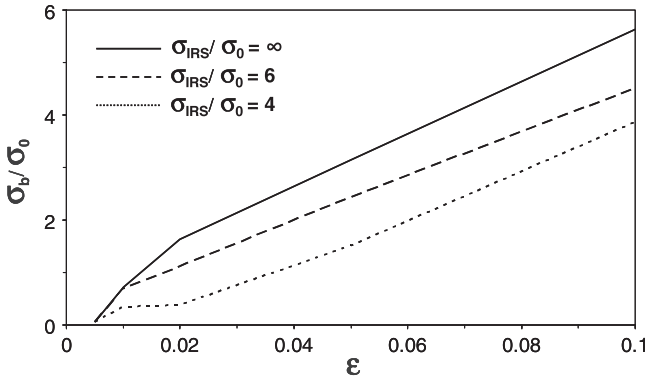

Fig. 11. Variation of the normalized back-stress σ_b/σ_0 as a function of the pre-strain: influence of the normalized interface relaxation stress σ_{IRS}/σ_0.

$$\sigma_b = \frac{\sigma_y^{forward} - \sigma_y^{backward}}{2} \tag{10}$$

where $\sigma_y^{forward}$ and $\sigma_y^{backward}$ correspond to the current yield stress upon loading and reverse loading, respectively. Fig. 11 shows the evolution of the normalized back-stress σ_b/σ_0 with the pre-strain ε for three values of the normalized interface relaxation stress σ_{IRS}/σ_0. The back-stress σ_b increases linearly with ε in agreement with Xiang and Vlassak, with an offset depending on σ_{IRS}: the larger the relaxation stress, the larger the back-stress. The magnitude of the predicted back-stress is, however, 2–3 times smaller than the experimental value. The underestimation comes from the fact that the model does not take into account additional sources of back-stress caused, for instance, by the grain size or crystal orientation distributions.

The ductility of 200 and 375 nm thick Al films has been recently characterized using a dedicated on-chip tensile testing technique [22]. Strong imperfection sensitivity related to the sample thickness and surface area has been observed. Indeed, there is an increasing probability of producing larger geometrical imperfections (e.g. inherent to the fabrication process) and material imperfections (e.g. due to the size and orientation distribution) when the surface area increases, as well as when the thickness decreases. The measured ductility varies between 0.016 and 0.08 for the 200 nm thick films, and between 0.07 and 0.27 for the 375 nm thick films. Using the same grain shape $d/h = 0.8$, a normalized interface relaxation stress $\sigma_{IRS}/\sigma_0 = 4$ and an internal length $l_* = 0.75\,\mu m$, the present model predicts a ductility equal to 0.063 and 0.092 for the 200 nm and 375 nm thick films, respectively. Considering an imperfection $\eta = 1\%$, the value for the 200 nm film is in good agreement with the experimental data, but the ductility of the 375 nm film is significantly underestimated. Furthermore, taking into account the experimental grain size distribution by decreasing η as in the previous section would lower the ductility even more. We anticipate that rate-sensitivity effects, connected to grain growth mechanisms, can, in this case, play a significant role and increase the ductility [50,51]. Further studies will aim at accounting for rate-sensitivity effects.

4. Conclusions

A finite-element model relying on a finite-strain implementation of the Fleck–Hutchinson strain gradient plasticity theory for the behavior of the grain interior, and on a representation of the interface layers as cohesive zones with evolving higher-order boundary conditions, has been presented and validated towards experimental results. The interface layers (grain boundary, interface with the substrate or with an oxide layer) are considered to be initially impenetrable to dislocations, but this constraint can be relaxed when the stress on an interface reaches a critical value. This model successfully captures

- the increase of strength with decreasing grain size, and with decreasing thickness in presence of constrained surfaces. When both strengthening effects are acting, equiaxed grains show a smaller strength than elongated and flat grains having the same total length of interfaces in the plane of deformation,
- the decrease of the uniform elongation with decreasing thickness and grain size, and with increasing imperfection. Allowing the relaxation of the higher-order boundary conditions leads to a more pronounced (and more realistic) loss of ductility. Grain size distribution is a significant source of imperfections,
- the accumulation of back-stress with pre-strain. The Bauschinger effect depends on the stress value up to which interface layers are impenetrable to dislocations.

All these trends are in fair agreement with the experimental data. Alternative approaches to model the same problem have been proposed in the literature, from simple 1-D dislocation-based formalisms [15] to sophisticated discrete dislocation dynamics simulations [12,13,34,35]. The present model offers a good trade-off with a relatively rigorous full constitutive model approach while limiting the number of parameters (one internal length and one relaxation stress on top of the hardening law) and allowing for finite-strain simulations of relatively complex systems. In order to account for rate-sensitivity effects, a viscoplastic formulation [52] of the present model will be implemented in the future.

Acknowledgements

The support of the Communauté Française de Belgique and of the Université catholique de Louvain through an ARC project, of the Region Wallonne for the project Winnomat II “Dinosaure”, and of the Belgian Science Policy through the IAP 6/24 project are gratefully acknowledged. The calculations were performed on the CISM-UCL, Belgium computer facilities.

References

[1] Lacour S, Wagner S, Huang Z, Suo Z. Appl Phys Lett 2003;82:2404.
[2] Sun Y, Rogers JA. Adv Mater 2007;19:1897.
[3] Béfahy S, Yunus S, Troosters M, Pardoen T, Bertrand P. Appl Phys Lett 2007;91:141911.
[4] Spearing SM. Acta Mater 2000;48:179.
[5] Iker F, Andre N, Pardoen T, Raskin J-P. J Microelectromech Syst 2006;15:1687.
[6] Evans AG, Hutchinson JW. Acta Mater 1995;43:2507.
[7] de Boer MP, DelRio FW, Baker MS. Acta Mater 2008;56:3344.
[8] de Boer MP, Corwin AD, Kotula PG, Baker MS, Michael JR, Subhash G, et al. Acta Mater 2008;56:3313.
[9] Haque MA, Saif MTA. Exp Mech 2003;43:248.
[10] Venkatraman R, Bravman JC. J Mater Res 1992;7(8):2040.
[11] Gruber PA, Böhm J, Onuseit F, Wanner A, Spolenak R, Arzt E. Acta Mater 2008;56:2318.
[12] Nicola L, Van der Giessen E, Needleman A. Philos Mag 2005;85:1507.
[13] Nicola L, Xiang Y, Vlassak JJ, Van der Giessen E, Needleman A. J Mech Phys Solids 2006;54(10):2089.
[14] Stolken JS, Evans AG. Acta Mater 1998;46:5109.
[15] Consonni V, Feuillet G, Gergaud P. Acta Mater 2008;56:6087.
[16] Pardoen T, Coulombier M, Boé A, Safi A, Brugger C, Ryelandt S, et al. Mater Sci Forum 2010;633–634:615.
[17] Fleck NA, Hutchinson JW. J Mech Phys Solids 2001;49:2245.
[18] Massart TJ, Pardoen T. Submitted for publication.
[19] Mazzoni-Leduc L, Pardoen T, Massart TJ. Int J Solids Struct 2008;45:5397.
[20] Xiang Y, Vlassak JJ. Acta Mater 2006;54:5449.
[21] Gravier S, Coulombier M, Safi A, André N, Boé A, Raskin J-P, et al. JMEMS 2009;18(3):555.
[22] Coulombier M, Boé A, Brugger C, Raskin J-P, Pardoen T. Scripta Mater 2010;62(10):742.
[23] Niordson CF, Tvergaard V. Int J Solids Struct 2005;42:2559.
[24] Niordson CF, Redanz P. J Mech Phys Solids 2004;52(11):2431.
[25] Evans AG, Hutchinson JW. Acta Mater 2009;57:1675.
[26] McMeeking RM, Rice JR. Int J Solids Struct 1975;11:601.
[27] Aifantis KE, Willis JR. Mech Mater 2006;38(8–10):702.
[28] Aifantis K, Soer W, De Hosson J, Willis JR. Acta Mater 2006;54:5077.
[29] Fleck NA, Willis JR. J Mech Phys Solids 2009;57(7):1045.
[30] Fleck NA, Willis JR. J Mech Phys Solids 2009;57(1):161.
[31] Abu Al-Rub RK. Int J Plast 2008;24:1277.
[32] Kocks UF, Mecking H. Progress Mater Sci 2003;48:171.
[33] Mazzoni-Leduc L, Pardoen T, Massart TJ. Eur J Mech A – Solids 2010;29:132.
[34] Nicola L, Van der Giessen E, Needleman A. J Appl Phys 2003;93:5920.
[35] Nicola L, Van der Giessen E, Needleman A. Thin Solid Films 2005;479:329.
[36] Li T, Huang ZY, Xi ZC, Lacour SP, Wagner S, Suo Z. Mech Mater 2005;37:261.
[37] Li T, Suo Z. Int J Solids Struct 2006;44:1696.
[38] Lu N, Wang X, Suo Z, Vlassak J. J Mater Res 2009;24:379.
[39] Lu N, Wang X, Suo Z, Vlassak J. Appl Phys Lett 2007;91:221909.
[40] Simar A, Brechet Y, de Meester B, Denquin A, Pardoen T. Acta Mater 2007;55:6133.
[41] Hall EO. Proc Phys Soc London, Sect B 1951;64:747.
[42] Petch NJ. J Iron Steel Inst London 1953;173:25.
[43] Dewald MP, Curtin WA. Modell Simul Mater Sci Eng 2007;15:S193.
[44] Dewald MP, Curtin WA. Philos Mag 2007;87:4615.
[45] Warner DH, Curtin WA. Acta Mater 2009;57:4267.
[46] Espinosa HD, Prorok BC, Peng B. J Mech Phys Solids 2004;52:667.
[47] Tsuchiya T, Hirata M, Chiba N, Udo R, Yoshitomi Y, Ando T, et al. J Microelectromech Syst 2005;14:903.
[48] Haque MA, Saif MTA. Acta Mater 2003;51:3053.
[49] Hutchinson JW, Neale KW. Acta Metall 1977;25:839.
[50] Gianola DS, Warner DH, Molinari JF, Hemker KJ. Scripta Mater 2006;55:649.
[51] Legros M, Gianola DS, Hemker KJ. Acta Mater 2008;56:3380.
[52] Legarth BN, Niordson C. Int J Plast 2010;26:149.